

The Seasonal Cycle of Significant Wave Height in the Ocean: Local vs Remote Forcing

Luke V. Colosi¹, Ana B. Villas Bôas¹, Sarah T. Gille¹

¹Scripps Institution of Oceanography, University of California San Diego, La Jolla, California

Key Points:

- Seasonal Wind Anomaly Regions occur in locations where the strongest winds do not coincide with the winter storm season.
- Local winds influence significant wave height within Seasonal Wind Anomaly Regions.
- Seasonal Wind Anomaly Regions in the Southern Hemisphere are less influenced by local winds than those in the Northern Hemisphere.

Corresponding author: Luke V. Colosi, lcolosi@ucsd.edu

12 **Abstract**

13 Significant wave height (SWH) stems from a combination of locally generated “wind-sea”
 14 and remotely generated “swell” waves. In the Northern and Southern Hemispheres, wave
 15 heights typically undergo a sinusoidal annual cycle, with larger SWH in winter in response
 16 to seasonal changes in high-latitude storm patterns that generate equatorward propa-
 17 gating swell. However, some locations deviate from this hemispheric-scale seasonal pat-
 18 tern in SWH. For example, in the California coastal region, local wind events occur in
 19 boreal spring and summer, leading to a wind speed (WSP) annual cycle with a distinct
 20 maximum in boreal spring and a corresponding local response in SWH. Here ocean re-
 21 gions with a WSP annual cycle reaching a maximum in late spring, summer, or early fall
 22 are designated as seasonal wind anomaly regions (SWARs). Intra-annual variability of
 23 surface gravity waves is analyzed globally using two decades of satellite-derived SWH
 24 and WSP data. The phasing of the WSP annual cycle is used as a metric to identify SWARs.
 25 Global maps of probability of swell based on wave age confirm that during the spring
 26 and summer months, locally forced waves are more statistically more likely in SWARs
 27 than in surrounding regions. The magnitude of the deviation in the SWH annual cycle
 28 is determined by the exposure to swell and characteristics of the wave field within the
 29 region. Local winds have a more identifiable impact on Northern Hemisphere SWARs
 30 than on Southern Hemisphere SWARs due to the larger seasonality of Northern Hemi-
 31 sphere winds.

32 **Plain Language Summary**

33 At the ocean surface, wave height can give insight into ocean-atmosphere interac-
 34 tions. Storms generate waves, which are known as swell when they propagate away from
 35 their point of origin. Swell waves account for most of the global ocean’s surface waves.
 36 They vary annually, with large waves in the winter and small waves in the summer, due
 37 to seasonal changes in high-latitude storm systems. In some coastal areas, including the
 38 coast of California, local wind effects cause exceptionally high wind speeds in late spring.
 39 These strong local winds result in large waves in springtime, separate from the global-
 40 scale winter maximum in swell waves. Places with strong local winds during the late spring,
 41 summer, and early fall, here referred to as seasonal wind anomaly regions (SWARs), are
 42 identified using global satellite observations of wave height and wind speed. Details vary
 43 by location. SWAR wave fields depend on the exposure to swell as well as the strength

44 of the local winds. Compared with Southern Hemisphere storms, Northern Hemisphere
 45 storms have a stronger winter peak, which means that local winds have a larger influence
 46 in Northern Hemisphere SWARs than in Southern Hemisphere SWARs.

47 1 Introduction

48 Surface gravity waves are fundamental to ocean-atmosphere interactions, and they
 49 mediate exchanges of momentum, heat, gasses, and energy (Cavaleri et al., 2012; Edson
 50 et al., 2007; Sullivan et al., 2004; Villas Bôas et al., 2019). The flux of momentum from
 51 the wind to the wave field is the principal generation mechanism of surface waves (Ardhuin,
 52 2020), which are commonly defined as having wave periods from 1 to 30 seconds (Munk,
 53 1951). These waves can propagate long distances across the oceans away from their gen-
 54 eration site (Snodgrass et al., 1966). The wave field in a particular location represents
 55 the superposition of locally forced waves, “wind-sea”, and remotely forced waves, “swell”
 56 (Sverdrup & Munk, 1947; Semedo et al., 2011; Jiang & Chen, 2013; Villas Bôas et al.,
 57 2017).

58 Previous studies of the wave climate have focused on the global scale, for exam-
 59 ple by exploring the large-scale temporal trends and climate modes of the global wind
 60 and wave fields (e.g., I. R. Young, 1999; I. Young et al., 2011; Stopa & Cheung, 2014;
 61 Stopa, 2019; Echevarria et al., 2019) or by separating the wave field into swell and wind-
 62 sea components (e.g., Jiang & Chen, 2013; Semedo et al., 2011; Zheng et al., 2016). Al-
 63 though some regional analyses of the wave climate have been performed (Villas Bôas et
 64 al., 2017; Semedo, 2018; I. R. Young et al., 2020), there remains a gap in our understand-
 65 ing of how local atmospheric conditions influence the variability of the wave field.

66 Additionally, previous research, including studies by Semedo et al. (2011), Zheng
 67 et al. (2016), and Semedo (2018), has relied on wave model hindcasts to look at the char-
 68 acteristics of the global wave field for swell and wind-seas. In the present study, our goal
 69 is to provide an alternative observation-driven approach for exploring the influence of
 70 locally and remotely forced waves on the wave field at the global and regional scales.

71 Villas Bôas et al. (2017) showed that regional-scale wind variability can cause de-
 72 viations in the seasonal cycle of significant wave height (SWH). They explored a distinct
 73 deviation occurring off the California coast due to a local wind phenomenon known as
 74 expansion fan winds, which are generated by a combination of atmospheric conditions

and coastal topography configuration (Winant et al., 1988). In the California Current region, expansion fan winds cause the wind speed (WSP) annual cycle to have a distinct maximum during late spring and early summer which lies outside the timing of the expected hemispheric-scale annual cycle. As a result, locally generated waves dominate the wave field up to 50% of the time during late spring and early summer, causing a seasonal augmentation in SWH relative to expected background SWH. Winant et al. (1988) hypothesized analogous wind events to be present in other oceanic regions that have coastal topography and atmospheric conditions similar to California and that may have similar wind speed annual cycle variability. These regions include the west coast of Australia, the coast of Namibia, the coast of Chile, the southern Caribbean sea, the northwest coast of Africa near Morocco, and the Arabian Sea near the tip of Somalia. This list includes eastern boundary current regions, monsoon regions, and regions significantly sheltered from remotely forced waves. Here, we refer to ocean regions that have a WSP annual cycle reaching a maximum during the late spring, summer, or early fall collectively as Seasonal Wind Anomaly Regions (SWARs). To our knowledge, there has been no exploration of the possible influence of regional-scale wind variability on the intra-annual variability of SWH in SWARs.

In this study, we identify SWARs globally and assess whether the seasonality seen in the California Current region is typical of other SWARs, characterized by local effects that are out of sync with high-latitude winter storms. Global-scale satellite observations of SWH and WSP from 1993 to 2015 are used to identify the WSP seasonal cycle, and SWARs are identified based on the timing of this cycle relative to the expected hemispheric-scale annual cycle of WSP. Implications for wave climate are then assessed from the relative timing of the WSP and SWH seasonal cycles. The work presented here contributes to the current understanding of the wave climate in regions that are partially dominated by wind-seas, which may have relevance for sea-state dependent air-sea fluxes (Villas Bôas et al., 2019), management of coastal resources, as well as shipping and navigation (Stopa, 2019; Ardhuin et al., 2019).

This paper is organized as follows: Section 2 describes the data sets and methods used to analyze global SWH and WSP. Section 3 explores the parameters of the annual and semi-annual SWH and WSP least-squares models globally and regional climatologies of potential expansion fan wind SWARs. This section also examines whether SWH

107 measurements during the late spring, summer or early fall months within SWARs are
 108 caused by locally or remotely generated waves. Section 4 summarizes our conclusions.

109 **2 Data and Methods**

110 **2.1 Remotely Sensed Data**

111 Wave data used in this study are drawn from over two decades (1 January 1993
 112 to 31 December 2015) of cross-calibrated satellite altimeter SWH measurements produced
 113 by the Institut français de recherche pour l'exploitation de la mer (IFREMER) (Queffeulou
 114 & Croizé-Fillon, 2017; Queffeulou, 2004). IFREMER's SWH altimeter data set ensures
 115 near homogeneity of SWH measurements between multiple near-pole non-sun-synchronous
 116 satellites, which are calibrated against buoy observations. Here, we binned the daily along-
 117 track data onto a 1° by 1° spatial grid. Satellites incorporated in this IFREMER prod-
 118 uct include ERS-1&2, TOPEX-Poseidon, GEOSAT Follow-ON, Jason-1, Jason-2, EN-
 119 VISAT, Cryosat and SARAL AltiKa (see Queffeulou & Croizé-Fillon, 2017; Queffeulou,
 120 2004).

121 Sea surface wind data were obtained from the Cross Calibrated Multi-Platform ver-
 122 sion 2 (CCMP2) wind vector analysis produced by Remote Sensing Systems (Atlas et
 123 al., 2011). CCMP2's data product is released on a 0.25° by 0.25° spatial grid with 6 hourly
 124 temporal resolution. For this analysis, we averaged CCMP2 winds spatially to a 1° by
 125 1° grid and temporally to daily resolution in order to match the gridded SWH data. The
 126 CCMP2 product incorporates measurements from scatterometers, radiometers, in situ
 127 buoys, and modelled wind velocity. CCMP2 provides zonal and meridional components
 128 of winds 10 meters above the sea surface, which are used to compute WSP (Atlas et al.,
 129 2011).

130 **2.2 WAVEWATCH 3 Model Hindcast**

131 To complement our satellite data analysis, we use a wave hindcast produced by IFRE-
 132 MER using the WAVE-height, WATer depth and Current Hindcasting III (WW3) wave
 133 model forced by Climate Forecast System Reanalysis (CFSR) winds. Simulations span
 134 the period from 1993 to 2015 and are output at 6 hourly temporal and 0.5° spatial res-
 135 olution. For model setup and validation, we refer the reader to Raschke and Arduin (2013).

136 In the supplementary material, we show our core analyses repeated with WW3 SWH and
 137 CFSR WSP (Figures S8-S9).

138 2.3 Monthly Climatology: Annual and Semi-Annual Variability

139 The analysis in this study focuses on annual and semi-annual variability as well as
 140 the mean states of the wave and wind fields using monthly averaged SWH and WSP. In
 141 order to analyze the annual and semi-annual variability, at each grid point, we perform
 142 a weighted least-squares fit to the mean, annual, and semi-annual cycles of SWH and WSP
 143 monthly climatologies. Annual and semi-annual cycles are represented as a sum of a sine
 144 and cosine, and fitted coefficients are used to infer amplitude and phase. Since 5 coef-
 145 ficients were least-squares fitted, IFREMER SWH grid locations were considered only
 146 if climatological means were available for at least 5 months of the year. In addition, to
 147 reduce errors associated with sparse sampling, we required that there be at least one cli-
 148 matological monthly mean in each of the four seasons. For weights, we use the standard
 149 error of the monthly climatology mean SWH and WSP. The number of independent ob-
 150 servations for each monthly climatology average was computed using the decorrelation
 151 time scale over each month of CCMP2 WSP and IFREMER SWH daily data. Decor-
 152 relation time scales are computed from integrals of the lagged covariance (e.g., Gille, 2005),
 153 as discussed in the supplementary material. As a metric to evaluate the least-squares
 154 fit, we use fraction of variance explained (FVE) (Draper & Smith, 1998), defined as:

$$155 \text{FVE} = 1 - \frac{\sum_{i=1}^N \left(\frac{y_i - f_i}{\delta y_i} \right)^2}{\sum_{i=1}^N \left(\frac{y_i - \mu}{\delta y_i} \right)^2}, \quad (1)$$

156 where y_i is the i^{th} monthly climatology mean data point with standard error δy_i , μ is
 157 the mean derived from the weighted least-squares fit of the data, and f_i is the i^{th} model
 158 value. Data and model are weighted in (1) for consistency with the weighted least-squares
 159 fit. Since the weights represent the standard error of the mean, uncertainties inferred from
 160 the least-squares fit (e.g. Press et al., 1992) can be interpreted as the standard error of
 161 the mean of each fitted coefficient. Statistical uncertainties of the amplitude are com-
 162 puted using error propagation and thus represent the standard error of the mean am-
 163 plitude. Amplitudes smaller than twice the standard error were judged not to be sta-
 164 tistically different from zero. At grid points where the amplitude is not statistically sig-
 165 nificant, the phase is considered not well defined. See Figure S2 for fractional uncertainty
 for SWH and WSP amplitude.

166 Maps of the mean and standard deviation of SWH and WSP daily data in December-
167 January-February (DJF) and in June-July-August (JJA) illustrate the seasonal evolu-
168 tion and variance of the data (Figure 1). Monthly SWH and WSP climatologies were
169 computed for candidate expansion fan regions identified by Winant et al. (1988) by spa-
170 tially averaging monthly climatologies and their variances within 4° by 4° regions. We
171 selected 4° by 4° regions with anomalously high WSP, small spatial WSP gradients, and
172 annual cycle phases corresponding to WSP maxima during the late spring, summer, or
173 early fall. To minimize the effects of land contamination and inaccurate tidal corrections
174 for satellite altimetry SWH data (Bouffard et al., 2008), 4° by 4° regions are at least 1°
175 of longitude and latitude away from the coast. Uncertainties for SWH and WSP monthly
176 climatologies were computed by dividing the standard deviation (σ) by $\sqrt{N_{\text{eff}}}$ where N_{eff}
177 is the number of degrees of freedom to obtain the standard error of the mean ($\sigma/\sqrt{N_{\text{eff}}}$).
178 We estimated N_{eff} by averaging monthly temporal decorrelation scales (n_d), represent-
179 ing the number of days between statistically independent measurements, into monthly
180 climatological averages, dividing the number of days of observations N used to compute
181 the monthly climatological average by the decorrelation scale such that $N_{\text{eff}} = N/n_d$,
182 and then spatially averaging N_{eff} over the 4° by 4° region.

183 Basin-scale SWH and WSP annual cycles were obtained for the Northern and South-
184 ern Hemispheres of the Pacific, Atlantic, and Indian Oceans through weighted least-squares
185 fits of the monthly climatologies (see Figure S4 for basin-scale mean climatologies and
186 annual cycle fits). In targeted study regions, we compare the regional SWH climatology
187 to the basin-scale SWH annual cycle. To do this, we assume that the phasing of the SWH
188 is determined on a basin-scale (largely by high-latitude storms) but that the mean SWH
189 and amplitude of the annual cycle can vary geographically. Thus we project the observed
190 local SWH onto the basin-scale fitted annual cycle. Differences between the two quan-
191 tify the deviation of the regional climatology from the expected hemispheric-scale an-
192 nual cycle.

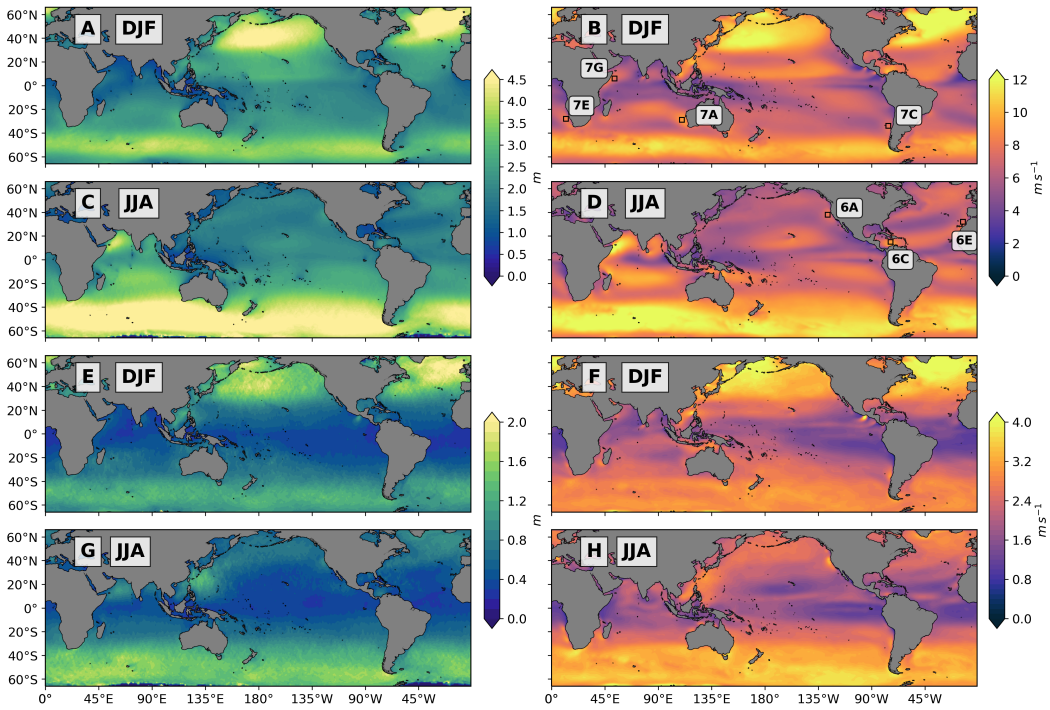


Figure 1. DJF seasonal mean for (A) IFREMER SWH and (B) CCMP2 WSP; JJA seasonal mean for (C) IFREMER SWH and (D) CCMP2 WSP; DJF standard deviation of daily data for (E) IFREMER SWH and (F) CCMP2 WSP; JJA standard deviation of daily data for (G) IFREMER SWH and (H) CCMP2 WSP. See text for details of computation. Black boxes in (B) and (D) indicate the selected regions for monthly climatology analysis in the Southern and Northern Hemispheres, respectively.

193

3 Results and Discussion

194

3.1 Annual and semi-annual cycles in wind speed and significant wave height

196

Phase maps show that generally SWH and WSP are in phase, with both reaching maxima in their annual cycles in winter in both hemispheres. An exception occurs in the northern Indian Ocean, which is sheltered from high-latitude Northern Hemisphere winter storms (Figure 2A,B). In many regions across the globe, including high-latitude oceans, the tropical Atlantic and Pacific, and the region north of New Zealand, the SWH and WSP annual cycles are roughly in phase, implying that maximum wave height coincides in time with maximum WSP. However, several regions stand out in Figure 2A,B as de-

197

198

199

200

201

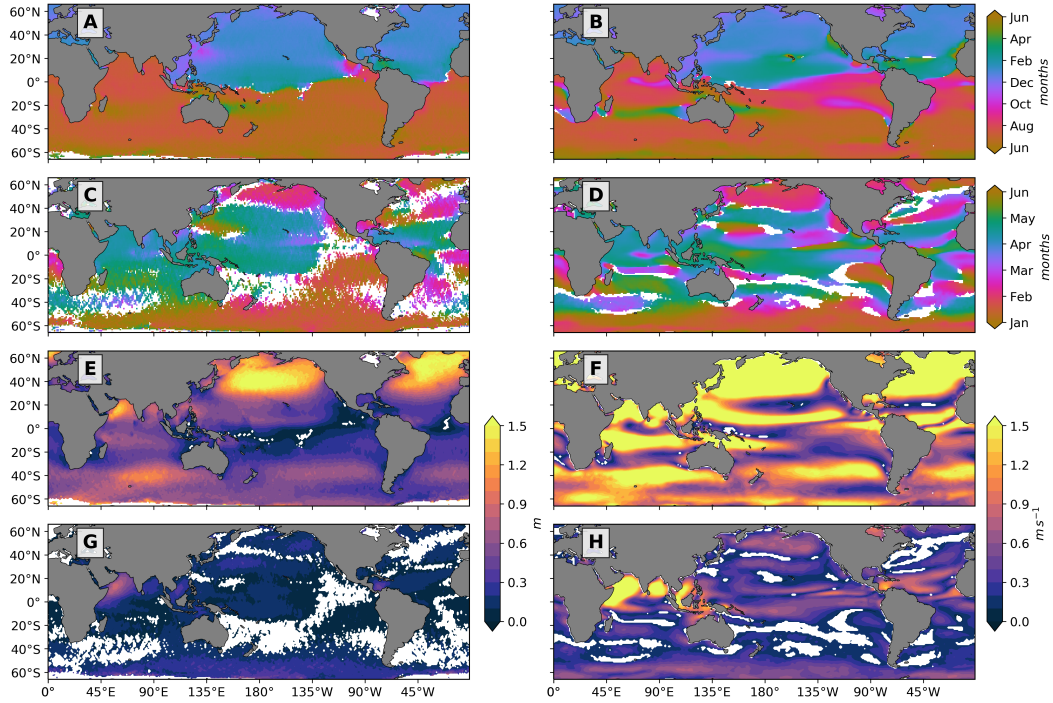


Figure 2. Phase of annual cycle for (A) IFREMER SWH and (B) CCMP2 WSP; phase of semi-annual cycle for (C) IFREMER SWH and (D) CCMP2 WSP; amplitude of annual cycle for (E) IFREMER SWH and (F) CCMP2 WSP; amplitude of semi-annual cycle for (G) IFREMER SWH and (H) CCMP2 WSP. Amplitudes less than or equal to twice the standard error are not considered statistically significant and masked white; the same pixels are also masked for phase. See section 2.3 for details of computation. Phase is indicated in months. Streak patterns in A, C, E, and G are an artifact of the altimeter sampling patterns and should not be interpreted as robust signal. (Comparison plots showing equivalent quantities for WW3 and IFREMER SWH and CFSR and CCMP2 WSP can be found in Figure S8 of the supplementary material).

203 viating from these general patterns, either because WSP or SWH do not peak in win-
204 ter or because WSP and SWH are out of phase with each other.

205 The annual cycle amplitude of both SWH and WSP (Figure 2E,F) is larger in the
206 high-latitude Northern Hemisphere than in the high-latitude Southern Hemisphere, im-
207 plying more seasonal variability in wave height and winds in the Northern Hemisphere
208 than in the Southern Hemisphere. However, mean SWH and WSP are consistently higher
209 in the Southern Hemisphere (Figure 1A-D). For SWH, high-amplitude annual cycles also
210 occur in the Arabian Sea and in zonal bands from $\sim 30^\circ\text{--}45^\circ$ in the Northern and South-

ern Hemispheres. In the tropical Pacific and Atlantic, the SWH amplitude drops to near zero, but the WSP annual amplitude does not approach zero in the same locations.

The semi-annual cycle phases for SWH and WSP (Figure 2C,D) have more spatial structure than the corresponding annual cycle phases. However, many grid points are judged not to be statistically significant (white pixels in Figure 2C,D). In regions with high-amplitude WSP and SWH semi-annual cycles, including the Arabian Sea, Bay of Bengal, South China, and Southern Caribbean, WSP and SWH are in phase, with phase values indicating maxima or minima occurring in April and October.

The SWH and WSP semi-annual cycle amplitudes are smaller in magnitude than the annual cycles (Figure 2G,H). For both WSP and SWH, the regions with the highest amplitude semi-annual cycles occur in the Arabian and Southern Caribbean Seas. The Bay of Bengal and the South China Sea have high amplitude only for WSP. The South Asian monsoon's semi-annual occurrence may play a role in strong semi-annual cycles, as the Arabian Sea, the Bay of Bengal, and the South China Sea are all monsoon regions.

Global maps of FVE (Figure 3A,B) assess the percentage of the variance explained by the mean plus annual and semi-annual cycles for SWH and WSP respectively. Features in the FVE maps for SWH and WSP align with features in the SWH and WSP annual and semi-annual amplitude maps (Figure 2): the percent of variation explained by the least-squares fit is highest in regions with high amplitude and lowest in regions of near zero amplitude or considered not statistically significant, with an exception for WSP off the coast of New Guinea. In locations where the annual and semi-annual cycles do not explain all of the temporal variability, local wind effects may be intermittent or simply governed by processes that are distinct from the annual and semi-annual cycle.

3.2 Waves: Swell Phase Discontinuities

In the equatorial Pacific and Atlantic, SWH phasing shows a sharp discontinuity between the Northern Hemisphere (boreal winter maximum) and the Southern Hemisphere (austral winter maximum) (Figure 2A). This phase transition, which we will refer to as a “swell phase discontinuity” occurs in regions of low to moderate seasonal mean SWH (Figure 1A,C) and low standard deviation (Figure 1E,G). It identifies the tran-

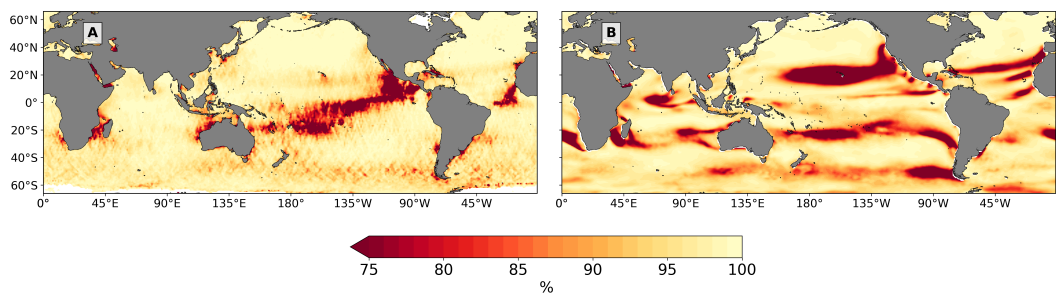


Figure 3. Fraction of variance explained by weighted annual and semi-annual least squares fit for IFREMER SWH (A) and CCMP2 WSP (B) from January 1st, 1993 to December 31st, 2015.

sition between regions with swell originating primarily in the Northern Hemisphere and swell primarily from the Southern Hemisphere. The swell phase discontinuity coincides geographically with “swell fronts” defined based on mean wave direction (I. R. Young, 1999; Semedo et al., 2011; Jiang & Chen, 2013). I. R. Young (1999) found that the Pacific and Atlantic swell front geographic locations vary seasonally. Since we define the swell phase discontinuity using SWH annual cycle phase, it represents an annually averaged signal that is expected to align with the annually averaged position of the swell front.

The swell phase discontinuity is slightly south of the equator in the western Pacific, between 5°S and 10°S west of 170°W, and it shifts equatorward further east (Figure 2A). In the Atlantic, the swell phase discontinuity aligns closely with the equator in the western Atlantic and abruptly shifts north of the equator near the western coast of Africa. Explanations for the geographic location of these boundaries are beyond the scope of the study and will be left for future research.

Just south of the swell phase discontinuity in the equatorial Pacific, several abrupt shifts in phase exist between 10°S and 20°S at approximately 180°E and 145°W. These are located on the northward facing sides of islands and are consistent with island shadowing: waves from the Southern Ocean propagating northward encounter the topography of Polynesian islands and are blocked from traveling any further north. As a result, waves vary with the Southern Hemisphere seasonal cycle to the south of the islands, and vary with the Northern Hemisphere seasonal cycle to the north of the island (see Figure S1 for an enlarged map of the SWH annual cycle phase in the Polynesian island region).

265 **3.3 Winds: Identifying Seasonal Wind Anomaly Regions**

266 The WSP annual-cycle phase, ϕ_{wsp} , allows us to identify atypical regions, where
 267 local winds are out of phase with hemispheric scale winds, providing a quantitative ap-
 268 proach to identify SWARs. We define a SWAR as a region with a statistically signifi-
 269 cant WSP annual cycle amplitude, with a phase that differs by 2.5 or more months from
 270 the expected WSP phase ϕ_{exp} set by hemispheric large-scale storm systems,

$$|\phi_{wsp} - \phi_{exp}| \geq 2.5 \text{ months.} \quad (2)$$

271 Assuming that ϕ_{exp} corresponds to a WSP annual cycle reaching a maximum during the
 272 middle of winter, mid-January in the Northern Hemisphere and mid-July in the South-
 273 ern Hemisphere, the criterion in (2) is fulfilled when the WSP maximum occurs roughly
 274 from April through October (boreal late spring, summer and early fall) for the North-
 275 ern Hemisphere and from October through April (austral late spring, summer, and early
 276 fall) for the Southern Hemisphere. Candidate SWARs determined by (2) are highlighted
 277 in Figure 4. (Figure S3 provides global maps of SWARs using alternate criteria.)

278 For this analysis, marginal seas and the equatorial regions across the Pacific and
 279 Atlantic Oceans are not considered. SWARs largely agree with the potential expansion
 280 fan regions identified by Winant et al. (1988) with the exception of the Arabian Sea. This
 281 metric also identifies some regions that were not suggested by Winant et al. (1988), in-
 282 cluding the Central North and South Atlantic, the Central West African coast off An-
 283 gola, the Southern Mozambique Channel, the North Indian Ocean, the Northwest and
 284 Eastern Australian coasts, Hawaii, the mid-latitude Southern Pacific, the Southern Mex-
 285 ican coast and multiple small coastal regions along the eastern South American coast.
 286 Table 1 categorizes candidate SWARs into three groups: expansion fan wind regions iden-
 287 tified by Winant et al. (1988), coastal regions, and open ocean regions. In the Southern
 288 Hemisphere, SWARs are concentrated in a zonal band from 15°S–30°S. From 66°S to
 289 66°N latitude, we found that SWARs constitute approximately 3.39% of the ocean's sur-
 290 face area. SWARs highlighted by this approach could be generated by a broad range of
 291 meteorological phenomena other than expansion fan wind events.

292 **3.4 Wind and Wave Relationships**

293 By comparing the timing of the annual cycle phases, ϕ_{swh} and ϕ_{wsp} , we explore the
 294 relationship between local winds and the regional wave field, as illustrated in Figure 5.

Table 1. Candidate SWARs, identified using Equation 2, with figure number of SWAR's regional climatology. Expansion Fan regions are identified by Winant et al. (1988).

Expansion Fan Regions	Coastal	Open Ocean
West Australian coast (7A)	Central West African coast (S7B)	Central North Atlantic (S6C)
Namibian coast (7G)	Southern Mozambique Channel (S7C)	Central South Atlantic (S7A)
Chilean coast (7C)	Northwest Australian coast	North Indian Ocean (S7E)
Southern Caribbean Sea (6C)	Eastern Australian coast (S7F)	Mid-latitude Southern Pacific (S7D)
Northwest African Coast (6E)	Hawaii (S6A)	
California Coast (6A)	Southern Mexican coast (S6B)	
	Eastern South American coast	

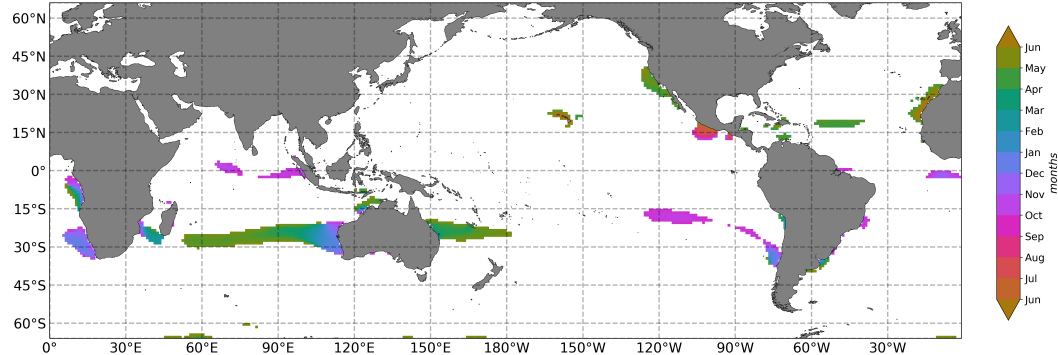


Figure 4. Annual cycle phase for CCMP2 wind speed, highlighting SWARs using the WSP maximum criteria. White pixels correspond to points that are not categorized as having anomalous phase or where the amplitude is not statistically significant.

In high latitudes, local winds are in phase with waves, consistent with storms generating waves. Near the swell phase discontinuity and in most SWAR regions, local winds and waves are out of phase. From 66°S to 66°N latitude, WSP and SWH phases differ by 0 to 1 months for 57.13% of the ocean's surface area, while phase differences range from $\pm 4\text{--}6$ months for 1.65% of the ocean's surface area.

Within SWARs, the relationship between WSP and SWH annual cycle phases shows the impact of local winds on the wave field. We find two types of relationships: (a) waves, aligned with hemispheric scale waves but out of phase with local winds and (b) waves, not aligned with hemispheric scale waves but in-phase with local winds.

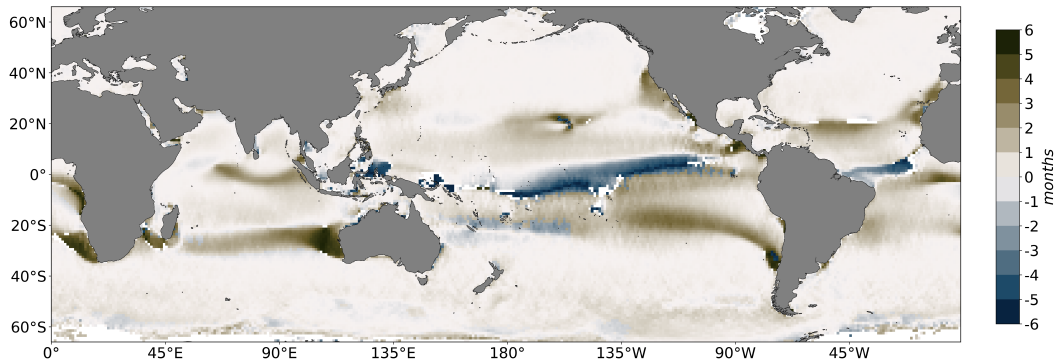


Figure 5. Difference between the annual cycle phases, ϕ_{wsp} and ϕ_{swh} . White pixels correspond to points where phase differences are not statistically significant, or where the annual cycle amplitude is small enough that phase is not well defined.

304 In most SWARs, ϕ_{swh} and ϕ_{wsp} differ by 2 to 6 months (Figure 5), so that mean
 305 WSP reaches a maximum when mean SWH is near its minimum. Villas Bôas et al. (2017)
 306 described such a phase relationship within the California Current SWAR, where the WSP
 307 maximum occurs during boreal spring or summer. Since annual cycles in SWH are usu-
 308 ally attributed to swell, high winds that are out of sync with high waves suggest the pos-
 309 sibility of strong locally forced wind waves that peak at a different time of year than the
 310 swell generated in the same hemisphere as the SWAR. SWARs thus have the potential
 311 to have SWH that deviates from the annual cycle typical of swell originating from high-
 312 latitude storms. However, observations reveal that the extent to which local winds in-
 313 fluence the wave field depends on regional wave and wind characteristics. Three char-
 314 acteristics of primary importance include exposure to swell generated in the high-latitude
 315 Northern or Southern Hemisphere, swell's annual cycle amplitude, and the strength of
 316 local winds. Among all SWARs, there are regions that have no exposure to Northern or
 317 Southern Hemisphere swell, regions with exposure to swell from one hemisphere, and re-
 318 gions with exposure to both Northern and Southern Hemisphere swell. Different com-
 319 binations of these three characteristics lead to local winds having varied impacts on the
 320 regional wave field. Deviations from the annual cycle could also be attributed to swell
 321 originating in the high latitudes of the opposite hemisphere such that contributions to
 322 SWH from opposing hemisphere swell is greater than locally generated wind-seas. Fur-
 323 thermore, compared with the Northern Hemisphere, the Southern Hemisphere's low SWH
 324 annual cycle amplitude (Figure 2E) provides relatively consistent swell, making regions

325 with significant exposure to the Southern Hemisphere experience less measurable influence
 326 from local winds.

327 Exceptions to the out-of-phase behavior in SWARs occur in the Arabian Sea, the
 328 Eastern Australian Coast, the South Mexican Coast, and the Southern Caribbean, where
 329 ϕ_{wsp} and ϕ_{swh} have a 0 to 1 month phase difference. This in-phase relationship, along
 330 with ϕ_{swh} reaching a maximum outside the timing of the expected hemispheric SWH an-
 331 nual cycle (Figure 2A), suggests that the waves within these SWARs are primarily lo-
 332 cally forced, with little impact from remotely-forced swell.

333 3.5 Regional Climatologies of SWARs

334 In order to examine how phasing differences in the SWH and WSP annual cycles
 335 influence wave fields within SWARs, monthly climatologies for SWH and WSP were com-
 336 puted in 4° by 4° grid boxes centered on a core portion of the SWAR. Here we focus on
 337 SWARs in the potential expansion fan regions identified by Winant et al. (1988). Re-
 338 gional climatologies for all other SWARs can be found in the supplementary material (see
 339 Figures S5–S7). Calculations use data from January 1st, 1993 to December 31st, 2015
 340 and focus on the individual boxes outlined in Figure 1B,D with enlarged maps in the left
 341 panels of Figures 6 and 7. The right panels of Figures 6 and 7 show SWAR regional cli-
 342 matologies for WSP (solid red) and SWH (solid blue) for the Northern and Southern Hem-
 343 spheres, with the hemispheric SWH mean annual cycle computed as an average for the
 344 ocean basin (blue dashed line) and the residual between SWH climatology and basin-
 345 scale annual cycle (black, with gray shading). In Figures 6 and 7, WSP and SWH cli-
 346 matologies show distinctly different patterns depending on region. On the basin-scale,
 347 with the exception of the Indian Ocean (which we will address separately), SWH and
 348 WSP exhibit nearly the same basin-scale annual cycles in each ocean basin (Figure S4).
 349 This means that regional deviations in SWH cannot be attributed to geographic vari-
 350 ations in basin-scale wind climatologies.

351 For Northern Hemisphere SWARs in eastern boundary current regions (i.e. the Cal-
 352 ifornia Current in Figure 6A-B and North Africa in Figure 6E-F), the sharp summer peak
 353 in the WSP climatology (red) coincides with an anomalous augmentation in SWH (blue)
 354 relative to the basin-scale annual cycle (blue dashed line). In both cases, the observed

355 augmentations deviate by more than twice the standard error from the basin-scale
 356 annual cycle.

357 In contrast, in the Southern Hemisphere eastern boundary current areas, with the
 358 exception of western Australia (i.e. the Chilean coast in Figure 7D-E and the Namib-
 359 ian coast in Figure 7F-G), we see broad summer increases in WSP extending from Oc-
 360 tober or November through February or March (red) that correspond to small magni-
 361 tude deviations of SWH (blue) of less than 0.5 standard errors from the basin-scale an-
 362 nual cycle. These results imply that in Southern Hemisphere SWARs (Figure 7), local
 363 winds have comparatively less influence on the wave climate than in the Northern Hemis-
 364 phere, possibly because strong year-round winds in the high-latitude Southern Hemis-
 365 phere lead to a smaller seasonal cycle in Southern Hemisphere swell (Figure 2A) and
 366 more overall wave energy than in the Northern Hemisphere. Against this background
 367 level of wind and swell, locally-induced anomalies in the Southern Hemisphere are ex-
 368 pected to be less distinct than in the Northern Hemisphere. The Indian Ocean is unusual
 369 in displaying a basin-scale WSP maximum in the austral summer months in addition to
 370 an austral winter maximum, which complicates interpretation of processes governing SWAR
 371 WSP and SWH. Off the coast of Western Australia (Figure 7A-B), the summer WSP
 372 peak that extends from December to February is particularly strong and corresponds to
 373 a 0.38 m SWH deviation (more than 3 standard errors) from the Indian Ocean's annual
 374 cycle. This is near the same magnitude as deviations in the Northern Hemisphere, sug-
 375 gesting that Western Australia's local winds are strong enough to influence the wave field
 376 at a level similar to Northern Hemisphere SWARs. The basin-scale WSP local maximum
 377 during austral summer may also play a role in determining the magnitude of the devi-
 378 ation.

379 The monsoon region in the Arabian Sea (Figure 7G-H) and the tropical storm re-
 380 gion in the southern Caribbean Sea (Figure 6C-D) have distinctly different wind and wave
 381 climatologies than the eastern boundary current regions. Both regions are characterized
 382 by strong semi-annual cycles in WSP (red lines in Figures 6D and 7H), and by SWH that
 383 varies with the semi-annual WSP (blue lines in Figures 6D and 7H). In the Caribbean,
 384 SWH shows almost no annual cycle (blue dotted line in Figure 6D), and in the Arabian
 385 Sea the annual cycle in SWH captures only a portion of the overall SWH variability. In
 386 both regions, the significance of the SWH semi-annual cycle compared with the annual
 387 cycle is demonstrated by the large deviations from the annual cycle (gray shading in Fig-

ures 6D and 7H). These patterns imply that semi-annually varying local winds are important drivers of SWH in these regions. The Antilles archipelago shelters the Southern Caribbean SWAR from waves propagating from high latitudes (Semedo et al., 2011) (Figure 6C). The lack of annual cycle in the SWH is consistent with the hypothesis that Caribbean SWH is forced entirely by local winds. In contrast, the Arabian Sea is not fully sheltered from remotely generated swell, and Indian Ocean WSP has a distinct pattern of semi-annual variability, meaning that SWH in the Arabian Sea could result from a combination of locally forced wind waves and remotely forced swell.

3.6 Wind-sea vs. Swell Dominance in SWARs

The phase differences and climatologies discussed in the preceding sections suggest the likely distinctions between remotely forced swell and locally forced wind waves. Phase differences between local SWH and hemispheric wind and wave climatologies can also occur if a region has significant exposure to swell propagating from the opposite hemisphere.

One method to distinguish swell from wind-sea is through wave age, which quantifies the stage of development of waves (Alves et al., 2003). Here we use the wave age criterion of Donelan et al. (1992), defined as:

$$\text{Wave Age} = \frac{C_p}{U_{10}}, \quad (3)$$

where C_p is the phase speed at the peak frequency of the wave spectrum, and U_{10} is the wind speed at 10 m elevation. For $C_p/U_{10} \leq 1.2$, the wave field is considered to be dominated by wind-sea and highly coupled to the local winds, with wind still supplying momentum to waves. For $C_p/U_{10} > 1.2$, the wave field is considered to be dominated by swell, where waves travelling 20% faster than U_{10} are outrunning the wind and not receiving momentum from the wind. For deep water waves, which are the focus of this paper, with peak frequency f_p , the dispersion relationship yields the peak phase speed:

$$C_p = \frac{g}{2\pi f_p}. \quad (4)$$

The wave field can be composed of a superposition of multiple wave systems. The peak phase speed represents the phase speed of the most energetic wave system. Thus, although both swell and wind-sea are likely to co-exist in the wave field, the separation process categorizes the wave field as being dominated either by swell or by wind-sea waves.

416 Using wave age, probability of swell can be obtained to estimate the fraction of time
 417 that the wave field is swell-dominated relative to the total number of wave measurements:

$$\text{Probability of swell} = \frac{N_{swell}}{N_{total}}, \quad (5)$$

418 where N_{swell} is the number of observations with wave age exceeding 1.2 representing a
 419 swell-dominated wave field and N_{total} is the total number of observations in the time se-
 420 ries. Probability of swell provides a metric to evaluate whether the atypical wind clima-
 421 tology within a SWAR is responsible for wind-seas during the late spring, summer, and
 422 early fall.

423 Previous global estimates of probability of swell (Semedo et al., 2011; Jiang & Chen,
 424 2013; Zheng et al., 2016) have shown that remotely forced waves dominate the wave field
 425 in all ocean basins with the exception the Southern Ocean, some coastal regions, and com-
 426 mon storm tracks, where wind-generated waves play a stronger role. Here, we comple-
 427 ment their results by focusing on regional analysis of SWARs. For probability of swell
 428 calculations we use WW3 SWH. Figures S8-S9 in the supplementary material show that
 429 WW3 SWH annual cycles resemble IFREMER SWH annual cycles.

430 The seasonal progression of probability of swell computed using C_p and U_{10} from
 431 the WW3 hindcast (Figure 8) is consistent with the findings of Semedo et al. (2011). First
 432 we consider the expansion fan SWARs identified by Winant et al. (1988). In these re-
 433 gions, the wave field is dominated by wind-seas a higher percentage of time than it is in
 434 surrounding regions. Wind-seas occur most typically during the late spring and early sum-
 435 mer months (Figure 8A,C). For the Northern Hemisphere, off the coasts of California
 436 and North Africa, the probability of swell drops to 80%–90% in spring and 60%–70% in
 437 summer. The Caribbean Sea has probabilities of swell below 75% through the entire year,
 438 with typical values ranging from 20%–40%, suggesting that the wave field consistently
 439 experiences stronger influence from local winds than most regions. In the Southern Hemis-
 440 phere, the probability of swell in the SWARs of West Australia, Chile, and Namibia ranges
 441 from 90% to 95%, which is not as low as in Northern Hemisphere SWARs. In the Ara-
 442 bian Sea, probability of swell drops to 60%–70% in the summer. These results are con-
 443 sistent with the hypothesis that the deviation from the basin-scale SWH annual cycle
 444 in SWARs results from locally forced wave contributions to SWH. The results also sup-
 445 port the hypothesis that compared with the Northern Hemisphere SWARs, Southern Hemi-

446 sphere SWARs are less likely to be dominated by locally forced waves because of their
 447 close proximity to persistent swell originating from the Southern Ocean.

448 One region of interest is the small coastal SWAR off the southern coast of Brazil
 449 near Rio de Janeiro (Figure 4A,D), where the probability of swell drops below 75% dur-
 450 ing austral spring and summer. Although this SWAR was not identified by Winant et
 451 al. (1988), its low probability of swell during austral summer and its coastal location sug-
 452 gest that the region has characteristic traits of expansion fan wind regions and may in
 453 fact experience expansion fan winds despite being on a western boundary.

454 A second category of SWARs in Figure 4 were those not identified as expansion fan
 455 regions by Winant et al. (1988). In these areas, the wave field is dominated by swell a
 456 high percentage of the time during the late spring, summer and early fall. With the ex-
 457 ception of the Mexican coast, the probability of swell is 95%–100% in these SWARs. Off
 458 the Mexican coast, the probability of swell drops to 85%–90% in the boreal fall. This
 459 suggests that the regional wave and winds characteristics are unfavorable for wind-sea
 460 conditions in SWARs located in the open ocean and some coastal regions.

461 4 Conclusion

462 In this paper, we have explored waves and winds separately, examining the seasonal
 463 cycle of WSP and SWH and closely examining regions where the seasonal cycles of winds
 464 and waves deviate from the seasonal cycle typically seen in the surrounding ocean basins.
 465 Atypical wave seasonal cycles are found within the equatorial region, where we see a sharp
 466 SWH phase transition, referred to as a swell phase discontinuity. Atypical WSP seasonal
 467 cycles, out of phase with hemispheric-scale winds, are identified as SWARs and are lo-
 468 cated in eastern boundary current regions, monsoon regions, and regions significantly
 469 sheltered from remotely forced waves. In total, 3.39% of the world oceans from 66°S to
 470 66°N latitude experience anomalous WSP seasonal variability.

471 The wave response to local winds is investigated to determine whether the char-
 472 acteristic features of the wind and wave fields observed off the California coast by Villas Bôas
 473 et al. (2017) are present in other SWARs. We find that most SWARs exhibit a 2–6 month
 474 phase difference between WSP and SWH annual cycles. However, anomalous patterns
 475 of wind variability do not necessarily drive anomalous patterns of wave climatology. Within
 476 potential expansion fan SWARs identified by Winant et al. (1988), SWH deviates from

477 the SWH seasonal cycle in the Northern Hemisphere but shows a low-to-zero magnitude
 478 deviation in the Southern Hemisphere. Exceptions to these phasing patterns occur along
 479 the southern Mexican coast, in the South Caribbean, in monsoon regions, and on the
 480 Eastern Australian coast, where local winds dominate over hemispheric-scale seasonal
 481 wind patterns. In these regions, the wave climate is consistent with a response to local
 482 winds. While there are commonalities between SWARs, the fraction of wave variability
 483 attributed to local wind events varies depending on regional and wave field character-
 484 istics, suggesting that the statistics that define the coastal California SWAR are not uni-
 485 versal, and each SWAR varies in slightly different ways depending on local conditions.

486 Probability of swell is used as a diagnostic to distinguish locally forced waves from
 487 remotely-forced swell. Within SWARs associated with expansion fan winds, during spring
 488 and summer months, probability of swell is lower than in surrounding regions, imply-
 489 ing wind-seas and SWH due to locally forced winds. This supports the hypothesis that
 490 the deviation from the SWH annual cycle results from waves that are forced by local wind
 491 events.

492 We have presented a method to evaluate the relative importance of wind-sea and
 493 swell from mean behavior of the wave field without the need for directional wave spec-
 494 tra. Improved understanding of the SWH response to local wind events has the poten-
 495 tial to lead to more accurate model representations of the wave climate in SWARs. In
 496 the future, global observations of directional wave spectra from remote sensing platforms
 497 such as the Chinese-French Oceanography Satellite CFOSAT and other proposed Doppler
 498 oceanography mission concepts have the potential to further our understanding of the
 499 effects of local winds on the wave climate: the addition of direction and frequency in-
 500 formation would help to distinguish the roles of swell, wind-seas, and mixed seas in de-
 501 termining wave conditions under different wind regimes across the globe and to better
 502 quantify the contribution of local winds to regional wave climates.

503 Acknowledgments

504 This work was supported by the NASA SWOT (awards NNX16AH67G and 80NSSC20K1136)
 505 and Ocean Vector Winds Science Teams (award 80NSSC19K0059), by a NASA Earth
 506 and Space Science Fellowship awarded to Ana Villas Bôas, and by the Hiestand Schol-
 507 ars program. CCMP Version-2.0 vector wind analyses are produced by Remote Sensing
 508 Systems. Data are available at www.remss.com. We thank the French Research Insti-

tute for Exploitation of the Sea (IFREMER) for providing the satellite altimetry significant wave height data (<ftp://ftp.ifremer.fr/ifremer/cersat/products/swath/altimeters/waves>) and WAVEWATCH 3 hindcast (<ftp://ftp.ifremer.fr/ifremer/ww3/HINDCAST>). Intermediate data products including binned IFREMER SWH, decorrelation time scales, weighted least-squares fit parameters and uncertainties, and probability of swell produced from CCMP2, IFREMER, and WW3 products are available through the University of California, San Diego library.

516 References

- 517 Alves, J. H. G., Banner, M. L., & Young, I. R. (2003). Revisiting the Pierson–
 518 Moskowitz asymptotic limits for fully developed wind waves. *Journal of Phys-
 519 ical Oceanography*, 33(7), 1301–1323. doi: 10.1175/1520-0485(2003)033<1301:
 520 RTPALF>2.0.CO;2
- 521 Ardhuin, F. (2020). *Ocean waves in geosciences*. doi: 10.13140/RG.2.2.16019.78888/
 522 5
- 523 Ardhuin, F., Stopa, J. E., Chapron, B., Collard, F., Jensen, R. E., Johannessen, J.,
 524 ... others (2019). Observing sea states. *Frontiers in Marine Science*, 6, 124.
 525 doi: 10.3389/fmars.2019.00124
- 526 Atlas, R., Hoffman, R. N., Ardizzone, J., Leidner, S. M., Jusem, J. C., Smith,
 527 D. K., & Gombos, D. (2011). A cross-calibrated, multiplatform ocean sur-
 528 face wind velocity product for meteorological and oceanographic applica-
 529 tions. *Bulletin of the American Meteorological Society*, 92, 157–174. doi:
 530 10.1175/2010BAMS2946.1
- 531 Bouffard, J., Vignudelli, S., Cipollini, P., & Menard, Y. (2008). Exploiting the po-
 532 tential of an improved multission altimetric data set over the coastal ocean.
 533 *Geophysical Research Letters*, 35(10). doi: 10.1029/2008GL033488
- 534 Cavalieri, L., Fox-Kemper, B., & Hemer, M. (2012). Wind waves in the coupled cli-
 535 mate system. *Bulletin of the American Meteorological Society*, 93(11), 1651–
 536 1661. doi: 10.1175/BAMS-D-11-00170.1
- 537 Donelan, M., Skafel, M., Gruber, H., Liu, P., Schwab, D., & Venkatesh, S. (1992).
 538 On the growth rate of wind-generated waves. *Atmosphere-Ocean*, 30(3), 457–
 539 478. doi: 10.1080/07055900.1992.9649449
- 540 Draper, N. R., & Smith, H. (1998). *Applied regression analysis* (Vol. 326). John Wi-

- 541 ley & Sons. doi: 10.1002/9781118625590
- 542 Echevarria, E., Hemer, M., & Holbrook, N. (2019). Seasonal variability of the global
543 spectral wind wave climate. *Journal of Geophysical Research: Oceans*, 124(4),
544 2924–2939. doi: 10.1029/2018JC014620
- 545 Edson, J., Crawford, T., Crescenti, J., Farrar, T., Frew, N., Gerbi, G., ... others
546 (2007). The coupled boundary layers and air-sea transfer experiment in low
547 winds. *Bulletin of the American Meteorological Society*, 88(3), 341–356. doi:
548 10.1175/BAMS-88-3-341
- 549 Gille, S. T. (2005). Statistical characterization of zonal and meridional ocean wind
550 stress. *Journal of Atmospheric and Oceanic Technology*, 22(9), 1353–1372. doi:
551 10.1175/JTECH1789.1
- 552 Jiang, H., & Chen, G. (2013). A global view on the swell and wind sea climate by
553 the Jason-1 mission: A revisit. *Journal of Atmospheric and Oceanic Technol-
554 ogy*, 30(8), 1833–1841. doi: 10.1175/JTECH-D-12-00180.1
- 555 Munk, W. H. (1951). *Origin and generation of waves* (Tech. Rep.). La Jolla, CA,
556 USA: Scripps Institution of Oceanography.
- 557 Press, W. H., Teukolsky, S. A., Flannery, B. P., & Vetterling, W. T. (1992). *Numer-
558 ical recipes in fortran 77: volume 1, volume 1 of fortran numerical recipes: the
559 art of scientific computing*. Cambridge university press.
- 560 Quefférou, P. (2004). Long-term validation of wave height measurements
561 from altimeters. *Marine Geodesy*, 27(3-4), 495–510. doi: 10.1080/
562 01490410490883478
- 563 Quefférou, P., & Croizé-Fillon, D. (2017). *Global altimeter SWH data set* (Vol. 2;
564 Tech. Rep.). ZI de la Pointe du Diable, CS10070, 29280 Plouzané, France:
565 IFREMER.
- 566 Rascl, N., & Arduuin, F. (2013). A global wave parameter database for geophysical
567 applications. Part 2: Model validation with improved source term parameteri-
568 zation. *Ocean Modelling*, 70, 174–188. doi: 10.1016/j.ocemod.2012.12.001
- 569 Semedo, A. (2018, Mar). Seasonal variability of wind sea and swell waves climate
570 along the canary current: The local wind effect. *Journal of Marine Science
571 and Engineering*, 6(1), 28. doi: 10.3390/jmse6010028
- 572 Semedo, A., Sušelj, K., Rutgersson, A., & Sterl, A. (2011). A global view on the
573 wind sea and swell climate and variability from ERA-40. *Journal of Climate*,

- 574 24(5), 1461–1479. doi: 10.1175/2010JCLI3718.1
- 575 Snodgrass, F. E., Hasselmann, K. F., Miller, G. R., Munk, W. H., & Powers, W. H.
- 576 (1966). Propagation of ocean swell across the Pacific. *Philosophical Trans-*
- 577 *actions of the Royal Society of London. Series A, Mathematical and Physical*
- 578 *Sciences*, 259(1103), 431–497. doi: 10.1098/rsta.1966.0022
- 579 Stopa, J. E. (2019). Seasonality of wind speeds and wave heights from 30 years of
- 580 satellite altimetry. *Advances in Space Research*. doi: 10.1016/j.asr.2019.09
- 581 .057
- 582 Stopa, J. E., & Cheung, K. F. (2014). Periodicity and patterns of ocean wind and
- 583 wave climate. *Journal of Geophysical Research: Oceans*, 119(8), 5563–5584.
- 584 doi: 10.1002/2013JC009729
- 585 Sullivan, P. P., McWilliams, J. C., & Melville, W. K. (2004). The oceanic bound-
- 586 ary layer driven by wave breaking with stochastic variability. Part 1. Direct
- 587 numerical simulations. *Journal of Fluid Mechanics*, 507, 143–174. doi:
- 588 10.1017/S0022112004008882
- 589 Sverdrup, H. U., & Munk, W. H. (1947). *Wind, sea and swell: Theory of relations*
- 590 *for forecasting* (No. 303). Hydrographic Office. doi: 10.5962/bhl.title.38751
- 591 Villas Bôas, A. B., Ardhuin, F., Ayet, A., Bourassa, M. A., Brandt, P., Chapron,
- 592 B., ... others (2019). Integrated observations of global surface winds, cur-
- 593 rents, and waves: requirements and challenges for the next decade. *Frontiers in*
- 594 *Marine Science*, 6. doi: 10.3389/fmars.2019.00425
- 595 Villas Bôas, A. B., Gille, S. T., Mazloff, M. R., & Cornuelle, B. D. (2017). Charac-
- 596 terization of the deep water surface wave variability in the California Current
- 597 region. *Journal of Geophysical Research: Oceans*, 122(11), 8753–8769. doi:
- 598 10.1002/2017JC013280
- 599 Winant, C. D., Dorman, C. E., Friehe, C. A., & Beardsley, R. C. (1988). The marine
- 600 layer off northern California: An example of supercritical channel flow. *Journal*
- 601 *of the Atmospheric Sciences*, 45(23), 3588–3605. doi: 10.1175/1520-0469(1988)
- 602 045<3588:TMLONC>2.0.CO;2
- 603 Young, I., Zieger, S., & Babanin, A. V. (2011). Global trends in wind speed and
- 604 wave height. *Science*, 332(6028), 451–455. doi: 10.1126/science.1197219
- 605 Young, I. R. (1999). Seasonal variability of the global ocean wind and wave climate.
- 606 *International Journal of Climatology: A Journal of the Royal Meteorologi-*

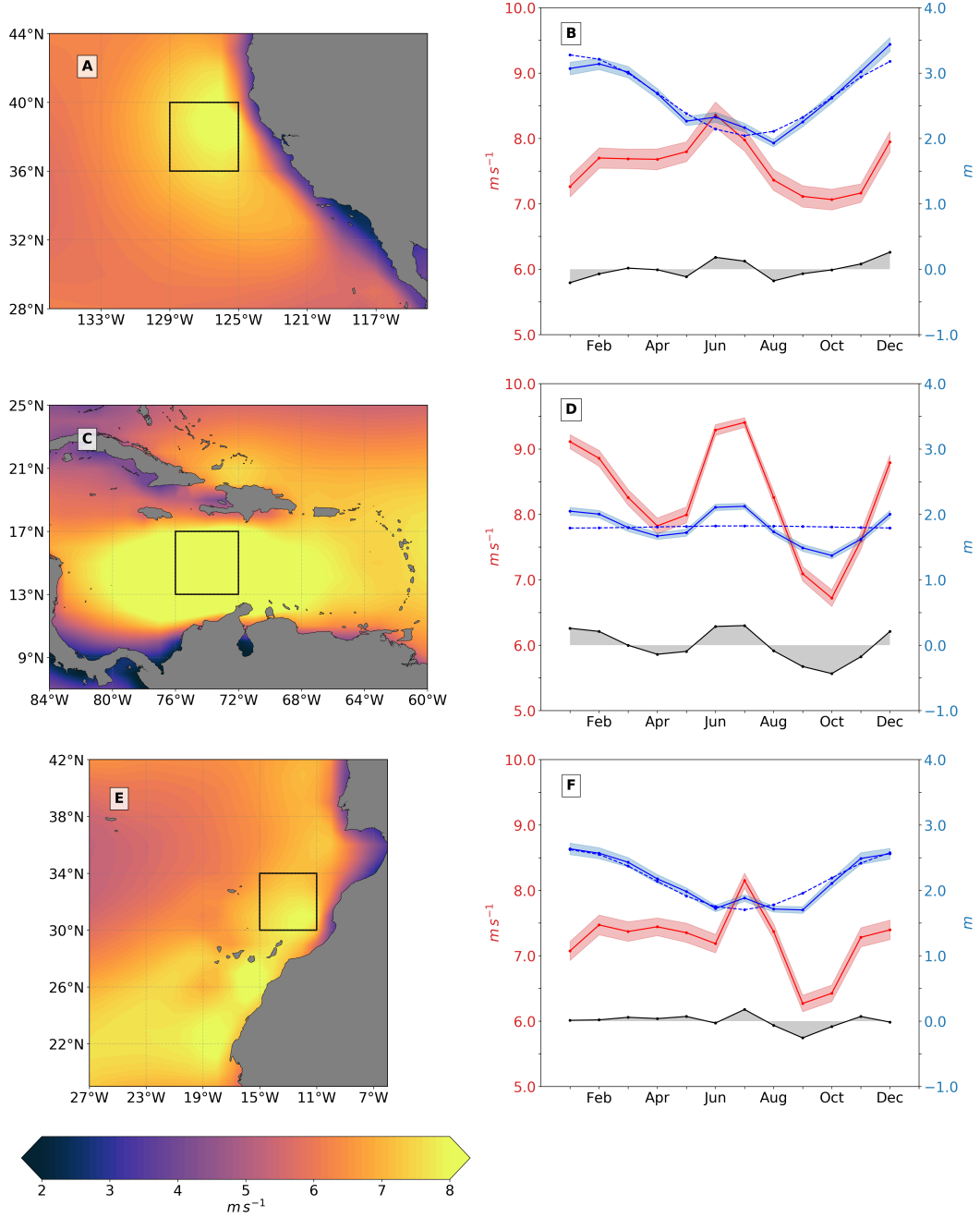


Figure 6. (left column) Northern Hemisphere wind speed in SWARs, averaged over June, July, and August. (right column) IFREMER SWH (solid blue) and CCMP2 WSP (solid red) climatologies extracted from the outlined 4° by 4° boxes within SWARs. Blue shading represents the standard error of the mean, dotted blue is the annual cycle weighted least-squares fitted to monthly climatology for mean SWH of the hemisphere ocean basin the SWAR is located in, and black solid is the residual between SWH regional climatology and annual cycle. SWARs include Northern California (A and B), Southern Caribbean Sea (C and D), and North Africa near the coast of Morocco and western Sahara (E and F). (Comparison plots showing equivalent quantities for WW3 and IFREMER SWH and CFSR and CCMP2 WSP can be found in Figure S9A,C,E of the supplementary material).

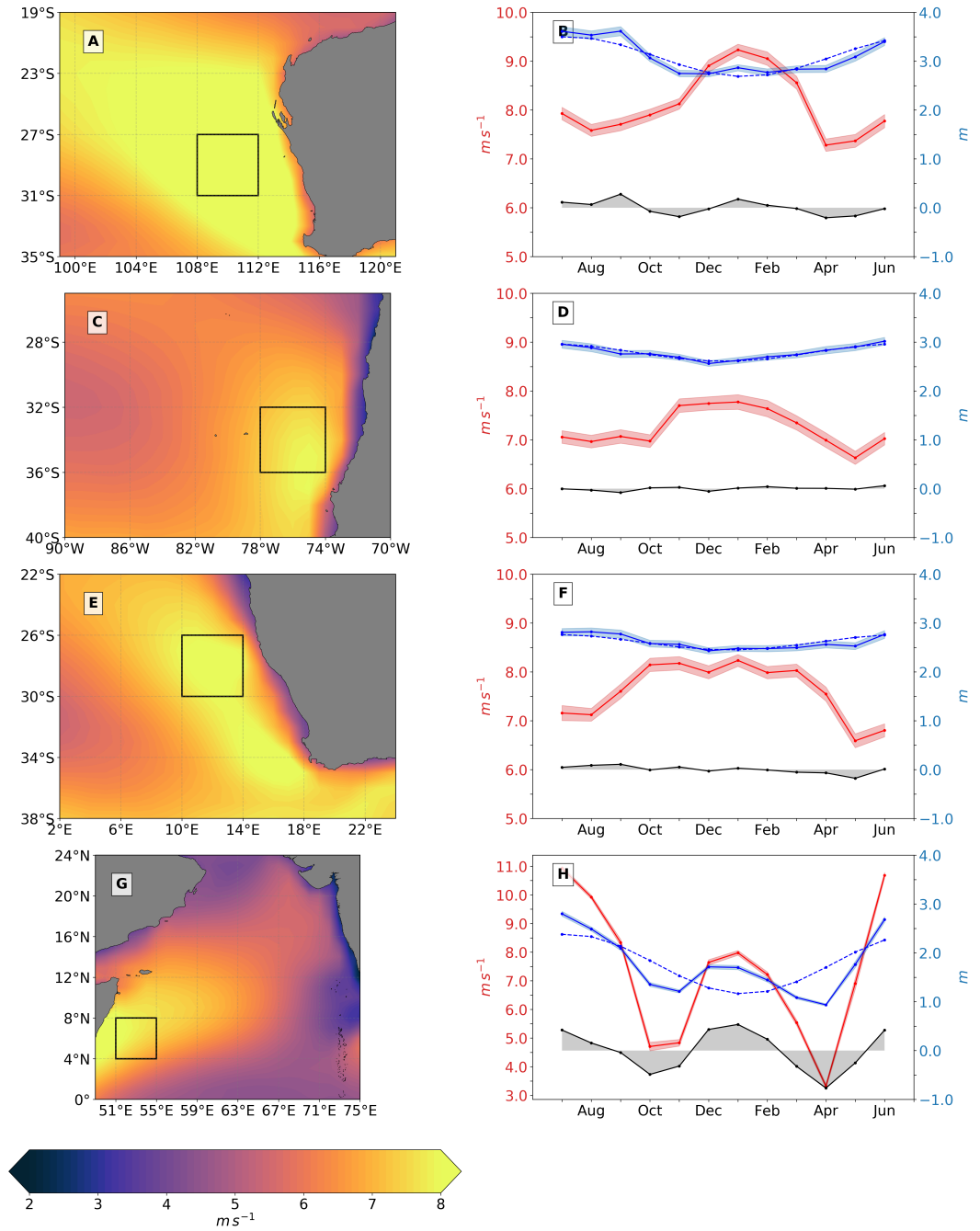


Figure 7. (left column) Southern Hemisphere wind speed in SWARs, averaged December, January, and February with (right column) IFREMER SWH (solid blue) and CCMP2 WSP (solid red) climatologies from the shaded 4° by 4° boxes. Shading, dotted lines, and solid black are as in Figure 6. SWARs include Western Australia (A and B), Central Western coast of South America near Chile (C and D), South-Western Coast of Africa near Namibia (E and F), and North-Western Arabian Sea (G and H). (Comparison plots showing equivalent quantities for WW3 and IFREMER SWH and CFSR and CCMP2 WSP can be found in Figure S9B,D,F,G of the supplementary material).

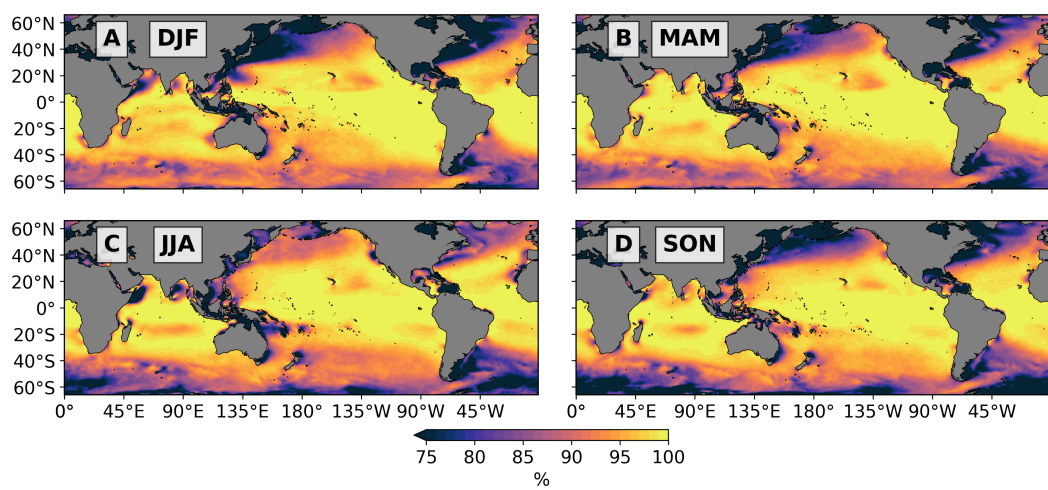


Figure 8. Seasonal progression of probability of swell using wave age criterion (3) and WW3 peak frequency and WSP from January 1st, 1993 to December 31st, 2015 where (A) DJF, (B) MAM, (C) JJA, and (D) SON